Radiation induced reduction of Graphene Oxide: a dose effect study

R

Souad Abou Zeid, [a] Selma Bencherif,[b] Rasta Ghasemi,[c] Rituporn Gogoi,[a,d] Yamina Chouli,[a] Matthieu Gervais,[e] Diana Dragoe,[f] Jalal Ghilane,[b] Prem Felix Siril [d] and Samy Remita *[a,g]

In this paper, we present a novel approach for the preparation of reduced Graphene oxide (rGO) through the radiolytical reduction of commercial Graphene Oxide (GO). The method is a highly efficient and environmentally friendly compared to other synthetic routes. We conducted a detailed study on the influence of absorbed doses during the synthesis process. The reduction process for the production of rGO is induced by the radiolysis of water at ambient temperature and pressure, confirmed by several sophisticated techniques. Our results demonstrate the efficiency of the radiolytical process compared to conventional methods of GO reduction. The C/O ratio increased from 3.3 (GO) to 11.2 (rGO), surpassing other reduction methods. Additionally, the ratio of intensities of D and G bands (ID/IG) increased for rGO due to an increase in order by reduction, implying the restoration of π-conjugation. Furthermore, the thermal stability of GO improved upon irradiation. Electrochemical measurements finally showed that our rGO exhibited a specific capacitance of 229.3 F g^{-1}, indicating its high potential as a candidate for energy storage applications.

1. Introduction

Pristine graphene (G), hailed as a transformative material of the 21st century, is distinguishable by its exceptional properties like mechanical strength, thermal and electrical conductivity, intriguing optical properties and more.[1,2] Such characteristics equip graphene for a wide array of applications, ranging from energy storage [3] and field-effect transistors [4] to biomedical utilities [5], sensor technology,[6] coatings,[7] optical devices,[8] catalysis,[9] and so on. Despite graphene's potential, the production of graphene sheets on a large scale and at an affordable cost remains a challenge, posing a barrier to its use in modern engineering and technology.[10] Initially isolated by mechanical exfoliation, this technique is not viable for mass production.[11] As researchers globally seek methods suitable for the scalable synthesis of graphene, various strategies have been explored such as epitaxial growth,[12] vapor deposition,[13] and liquid-phase exfoliation[14]. Despite the low quality of the produced graphene, reducing graphene oxide (GO) is a commonly employed technique for producing graphene, which is particularly useful for large-scale operations.[15] This process involves two main steps: the oxidation of pristine graphite into GO, and the subsequent reduction of GO into reduced graphene oxide (rGO). Although numerous reduction methods exist, including chemical,[16,17] thermal,[18,19] and electrochemical,[20] each comes with its own limitations, ranging from compromises in graphene's quality to environmental concerns associated with hazardous by products and energy-intensive processes.[21] For example, the chemical reduction process is highly scalable but can lead to unpredictable properties unlike pristine graphene.[22] The thermal heating of GO produces rGO with relatively better quality, although the process requires high reaction temperature and can damage the structure of the prepared rGO through the evolution of environmentally hostile gases like CO and CO_2, along with a substantial quantity of weight loss (30%).[21] Some of the challenges, mainly chemical purity, can be overcome via the electrochemical reduction process, which is also limited to large-scale production of rGO.[23]

[a] *Institut de Chimie Physique, ICP, UMR 8000, CNRS, Université Paris-Saclay, bâtiment 349, Campus d'Orsay, 15 avenue Jean Perrin, 91405 Orsay Cedex, France.*
[b] *Université de Paris, ITODYS, CNRS, UMR 7086, 15 rue J-A de Baïf, F-75013, Paris, France*
[c] *Institut d'Alembert, IDA, ENS Paris-Saclay, 4 avenue des sciences, 91190 Gif-sur-Yvette, France.*
[d] *School of Chemical Sciences, Indian Institute of Technology Mandi, Mandi, Himachal Pradesh-175005, India.*
[e] *Laboratoire Procédés et Ingénierie en Mécanique et Matériaux, PIMM, Arts et Métiers ParisTech, UMR 8006, CNRS, CNAM, HESAM université, 151 boulevard de l'hôpital, 75013 Paris, France.*
[f] *Institut de Chimie Moléculaire et des Matériaux d'Orsay, ICMMO, UMR 8182, CNRS, Université Paris-Saclay, bâtiment 410, Campus d'Orsay, Rue du doyen Georges Poitou, 91405, Orsay Cedex, France.*
[g] *Département Chimie Vivant Santé, EPN 7, Conservatoire National des Arts et Métiers, CNAM, 292 rue Saint-Martin, 75141 Paris Cedex 03, France.*
* *Corresponding author. Institut de Chimie Physique, ICP, UMR 8000, CNRS, Université Paris-Saclay, bâtiment 349, Campus d'Orsay, 15 avenue Jean Perrin,91405 Orsay Cedex, France. E-mail address: samy.remita@universite-paris-saclay.fr (Samy Remita).*

†Electronic Supplementary Information (ESI) available: [details of any supplementary information available should be included here]. See DOI: 10.1039/x0xx00000x

Unfortunately, the complete reduction of GO, essential for restoring the pristine properties of graphene, is complicated by residual oxygenated functional groups, such as carboxyl functionalities (located at the edges), epoxide groups (bridging oxygen atoms), hydroxyl groups (located in the basal plane), carbonyl, and organosulfate groups (as sulfur impurity), which impair the material's quality.[24]

Against this backdrop, a new horizon in graphene reduction has emerged: radiation-induced synthesis. This approach marries the economic and practical advantages of chemical methods with the high-purity output characteristic of physical techniques. To date, however, only a handful of studies have employed this approach, with UV light,[25] plasma,[26] xenon flash,[27] electron beams,[28] infrared (IR) photothermal reduction,[29] and Gamma (γ)-Rays,[30] cited as radiation (ionizing and nonionizing) sources. γ-ray irradiation, a high-frequency electromagnetic radiation stemming from nuclear decay, has proven advantageous in sterilization and materials processing thanks to its ability to operate without physical contact and its precision.[31] Over the last two decades, employing γ-rays has shown considerable promise in synthesizing colloidal metal nanoparticles, bimetallic clusters, conducting polymers and composites.[32–35] Notably, this process promotes the formation of uniform reducing agents and remains effective regardless of the presence of light-absorbing substances, also presenting an economical alternative to chemical and CVD methods.[34] γ-ray irradiation, especially in the synthesis of rGO from GO, achieves reduction at room temperature and negates the need for external reducing agents, thus highlighting its scalability and environmental benefits.[36] GO, typically suspended in water or water-alcohol mixtures, is subjected to gamma rays that induce the radiolysis of water,[37] producing both oxidative and reductive species that can facilitate the reduction process, particularly in presence of alcohols that serve as radical scavengers, eliminating oxidative $HO^{\bullet}$ and transforming it into reductive radicals.[38–40] Researchers have widely adopted this technique for synthesizing graphene and graphene-based materials, leading to a variety of applications. For the first time, Zhang et al. have reported the reduction of GO in a water/alcohol system using a dose rate of 0.88 kGy h^{-1} and a total absorbed dose of 35.3 kGy.[41] Furthermore, various materials, including 3D graphene aerogels,[30] rGO/Ni nanocomposites,[42] 3D graphene/Pt aerogel composites,[43] TiO_2-decorated rGO,[44] rGO/carbon nanotube composites,[45] rGO/organic inhibitor composites,[46] and composites of noble metal nanoparticles,[47] have been successfully synthesized using γ-ray irradiation. Additionally, GO has been effectively reduced in N,N-dimethylformamide (DMF) through high absorbed doses of γ-rays.[36,48]

It is important to acknowledge that the outcomes of gamma irradiation are subject to various influencing factors, including the irradiation conditions, the nature of the material under irradiation, and the specific medium utilized.[41,48–50] Notably, the dose rate plays a significant role in shaping the resulting product features.[51] For instance, an absorbed dose of 100 kGy has been observed to enhance the graphitization and surface properties of multi-walled carbon nanotubes (MWCNTs). However, higher doses may lead to structural damage, potentially resulting in the formation of diamond-like structures and carbon oxides.[50] Moreover, the effect of γ-irradiation at a dose rate of 3 kGy h^{-1} and an absorbed dose of 60–150 kGy on graphene with few layers has been investigated.[49]

Importantly, the present study aims to elucidate the γ-irradiation induced synthesis of rGO through the reduction of GO in water, using a dose rate of 3.3 kGy h^{-1} for a total absorbed dose ranging from 1 to 50 kGy, as illustrated in **Figure 1**. Our particular focus lies in determining for the first time in literature the radiolytic yield (G-value) of rGO. To the best of our knowledge, this investigation represents one of the comprehensive reports delineating the detailed impact of absorbed dose in the γ-irradiation-induced reduction of GO, particularly in an aqueous medium recognized for its benign nature. In addition, as it will be demonstrated, the radiolytically produced rGO not only shows promise for supercapacitor applications but also demonstrates excellent compatibility with a broad range of solvents, underscoring its potential for the same various applications suitable for graphene use, like composite materials, conductive inks, sensors and more.

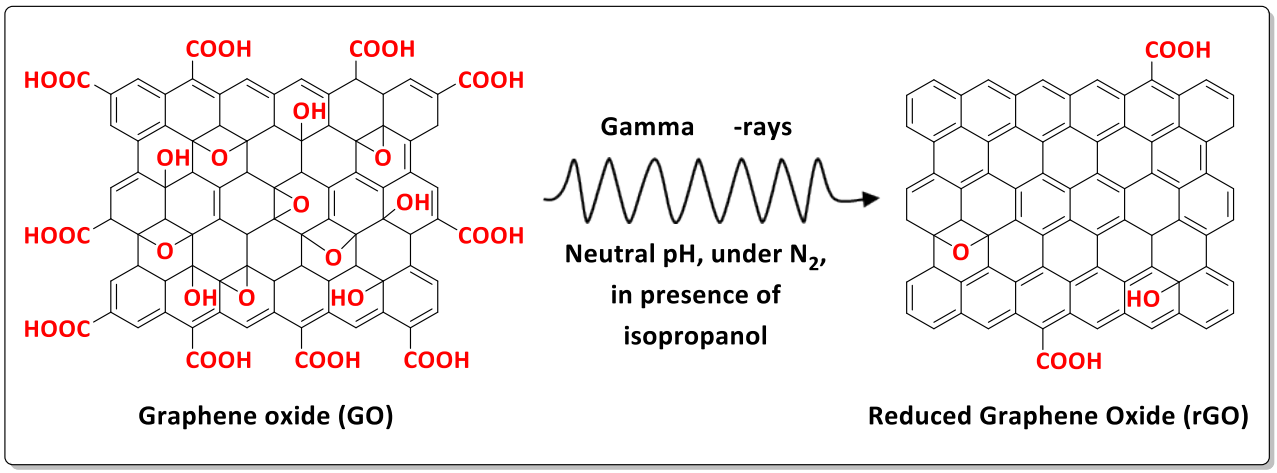

Figure 1 Schemat c representat on of rad o yt c synthes s of rGO n water

2. Materials and methods

2.1 Materials and reagents

Aqueous dispersion of graphene oxide (GO, 4 mg mL^{-1}) and potassium hydroxide (KOH, ≥85%) were purchased from Sigma-Aldrich. Ethylene glycol was obtained from EMPLURA®, and cyclohexane (C_6H_{12}, ≥99.5%) was sourced from VWR Chemicals. All organic solvents were procured from Sigma-Aldrich: isopropanol (IPA) (C_3H_8O, ≥95%), tert-Butanol (*t*-BuOH) ($C_4H_{10}O$, ≥95%), N,N-Dimethylformamide (DMF, ≥99%), diethyl carbonate (DEC, 99%), dimethyl sulfoxide (DMSO, ≥99.7%), toluene ($C_6H_5CH_3$, 99.8%), anhydrous 1,4-dioxane ($C_4H_8O_2$, 99.8%), tetrahydrofuran (THF, ≥99.9%), isopropyl alcohol (IPA, 99.5%), 1-chloropentane ($C_5H_{11}Cl$, 99%), anhydrous dichloromethane (DCM, ≥99.8%), n-butylamine ($C_4H_{11}N$, ≥99%), cyclohexanone ($C_6H_{10}O$, 99.8%), hexadecane ($C_{16}H_{34}$, ≥99%), acetylacetone ($C_5H_8O_2$, ≥99.9%), acetone (C_3H_6O, ≥99.5%), and ethanol (C_2H_5OH, 98%). Nitrogen (N_2) gas with 99.99% purity was obtained from Air Liquid Co. The Nafion® D-520 dispersion (5% w/w in water and 1-propanol, ≥1.00 meq g^{-1} exchange capacity) was purchased from Alfa Aesar. Deionized water (DI) with a Millipore system producing 18.2 Ω cm^{-1} was used as the solvent for all the experiments unless otherwise specified. The chemicals were utilized as received without further purification prior to the experiments.

2.2 Irradiation source

The irradiation source used in the study was a ^{60}Co γ-source with a strength of 3000 Curie (Ci), located at Institut de Chimie Physique, in Paris-Saclay university. The γ-source is securely stored in a lead jar and is raised mechanically for irradiation under operator control.

During the irradiation process, all glass vials containing aqueous solutions were positioned on a plate at fixed locations. The intensity of the irradiation was quantified by the absorbed dose (D), which measures the amount of energy deposited in the irradiated solution (in this case, aqueous solutions). This unit is expressed in grays (Gy), where 1 Gray is equivalent to one joule absorbed per kilogram of irradiated material (1 J kg^{-1} or 1 J L^{-1} for diluted aqueous solutions).[52] Additionally, the amount of energy deposited per unit of time is known as the dose rate (Gy h^{-1}).

The dose rates, ranging from 0,21 to 4,27 kGy h^{-1}, at different positions depend on the distance between the sample and the source and are determined by Fricke's dosimetry.[53]

2.3 Solution preparation

The commercial GO suspension was thoroughly shaken prior to use, and then left undisturbed for 5 hours to ensure no sedimentation before irradiation.

A modified approach, based on established literature procedures, was employed for the synthesis of rGO.[54] In a detailed account of the procedure, starting from commercial GO suspension, an aqueous solution with a concentration of 0.2 g L^{-1} of GO was prepared within a transparent glass vial (40 mL, 3 cm × 8 cm). This GO suspension was then further added with 0.2 mol L^{-1} isopropanol (IPA) or alternatively with 0.2 mol L^{-1} tert-Butanol. To eliminate the presence of dissolved oxygen that could potentially inhibit the reduction process, the GO solution was subjected to a degassing process with N_2 gas for 20 minutes. Subsequently, the degassed solution was exposed to gamma irradiation emanating from the previously described ^{60}Co γ-source. The absorbed dose ranged from 0 to 50 kGy at a dose rate of 3.33 kGy h^{-1}, performed under standard conditions of ambient temperature and atmospheric pressure.

2.4 Solution irradiation and GO reduction

The process of water radiolysis involves the dissociation of water molecules by ionizing radiation, leading to the production of various reactive (oxidizing and reducing) species. These include hydrated electrons (e^-_{aq}), hydroxyl radicals ($HO^\bullet$), hydrogen atoms ($H^\bullet$), hydroperoxyl radicals ($HO_2^\bullet$), hydronium ions (H_3O^+), hydroxide anions (HO^-), hydrogen peroxide (H_2O_2), and molecular hydrogen (H_2), as depicted in equation (1):[37,39,55,56]

$$H_2O \xrightarrow{\text{ionizing radiation}} e^-_{aq}, HO^\bullet, H^\bullet, HO_2^\bullet, H_3O^+, HO^-, H_2O_2, H_2 \qquad \textbf{Eq.1}$$

Nevertheless, at neutral pH, the radiolysis of water predominantly yields the species portrayed by equation (2):[57]

$$H_2O \xrightarrow{\text{ionizing radiation}} e^-_{aq}, HO^\bullet, H^\bullet, H_3O^+, HO^-, H_2O_2, H_2 \qquad \textbf{Eq.2}$$

The radiolytic yields (quantifying the amounts of molecules or free radicals generated or lost per 1 Joule of deposited energy) are established for different species resulting from water radiolysis at neutral pH: $G(HO^\bullet) = 2.8 \times 10^{-7}$ mol J^{-1}, $G(H^\bullet) = 0.6 \times 10^{-7}$ mol J^{-1}, and $G(e^-_{aq}) = 2.8 \times 10^{-7}$ mol J^{-1} for $HO^\bullet$, $H^\bullet$, and e^-_{aq}, respectively. These reactive species initiate chemical transformations in the irradiated system. Notably, e^-_{aq} and $H^\bullet$ are potent reducers, with standard reduction potentials $E°\ (H_2O/e^-_{aq})$ = -2.9 V_{NHE} and $E°\ (H^+/H^\bullet)$ = -2.3 V_{NHE}, respectively.[37,55,57] Conversely, $HO^\bullet$ radicals are strong oxidants with a standard redox potential $E°(HO^\bullet/H_2O)$ = +2.7 V_{NHE}.

Furthermore, the concentration of a reactive species produced by water (density (d)= 1 kg L^{-1}) radiolysis, C (mol L^{-1}), can be expressed as a function of the absorbed dose, D(Gy) and its radiolytic yield, G (mol J^{-1}) by using equation (3):

$$C\ (\text{mol } L^{-1}) = D\ (\text{Gy}) \times G\ (\text{mol } J^{-1}) \times d\ (\text{kg } L^{-1}) \qquad \textbf{Eq.3}$$

Conversely, the initial yield of disappearance of a solute upon radiolysis can be easily deduced from this equation by measuring the variation of its initial concentration as a function of the absorbed dose. Moreover, by using this equation, the required dose for the total consumption of a solute can also be calculated knowing its yield of disappearance.

When γ-irradiation is employed for the reduction of GO, it is crucial to selectively generate reducing species while minimizing the formation of oxidizers. For this purpose, added

IPA acts as a scavenger of $HO^{\bullet}$ and $H^{\bullet}$ radicals, converting them into the isopropanol radical ($(CH_3)_2C^{\bullet}OH$) through reactions (4) and (5):

$$(CH_3)_2CHOH + HO^{\bullet} \longrightarrow (CH_3)_2C^{\bullet}OH + H_2O \quad \textbf{Eq.4}$$

$$(CH_3)_2CHOH + H^{\bullet} \longrightarrow (CH_3)_2C^{\bullet}OH + H_2 \quad \textbf{Eq.5}$$

Isopropanol radicals are strong reducing agents with a standard potential of $E°$ ($(CH_3)_2CHOH/ (CH_3)_2C^{\bullet}OH$) = -1.8 VNHE at neutral pH.[58,59]

In summary, radiolysis of water in the presence of isopropanol under N_2 yields two potential reducing species e^-_{aq} with $G(e^-_{aq}) = 2.8 \times 10^{-7}$ mol J^{-1} and $(CH_3)_2C^{\bullet}OH$ with $G((CH_3)_2C^{\bullet}OH = G(HO^{\bullet}) + G(H^{\bullet}) = 3.4 \times 10^{-7}$ mol J^{-1}.[60] Together, these species should enable the efficient reduction of GO in aqueous medium into reduced graphene oxide, rGO.

2.5 Characterization of rGO

Following irradiation, rGO products were isolated via centrifugation at 7000 rpm for 15 minutes. To complete the process, rGO products were transferred to a hot-air oven, set at a temperature of 100°C, where they were left overnight to ensure thorough drying and the attainment of the final solid rGO products. Solutions (after and before irradiation) as well as dried solid products were then both characterized by complementary techniques.

UV-visible absorption spectra of the solutions were collected using an Agilent/HP 8453 UV-Vis spectrophotometer with a quartz cell featuring an optical path length of 2 mm. The absorption spectra were acquired in the optical range of 200-1200 nm with reference to DI water.

Fourier transform infrared (FTIR) spectra of the solid samples were recorded on a Bruker Vertex 70 spectrometer. The powdered samples were placed on a diamond crystal attached ATR plate (Pike MIRacle™ crystal plate diamond/ZnSe) and scanned in the range of 4000-600 cm^{-1} using a mercury cadmium telluride (MCT) detector integrated with a cooling system (liquid nitrogen).

Raman spectra of the solid samples were recorded by LabRAM HR800 (HORIBA Scientific, Jobin-Yvon) using a λ= 532 nm laser set at a power of 1 mW. This was carried out with a 100X objective lens and 0.9 NA.

X-Ray Photoelectron Spectroscopy (XPS) analysis of the solid samples was conducted on a Thermo Fisher Scientific K-Alpha instrument with a base pressure of about 5 x 10^{-9} mbar. It was equipped with an Al Kα monochromatic X-ray source ($h\nu$= 1486.6 eV) using the 400 µm spot size. The hemispherical analyzer was operated in CAE (Constant Analyzer Energy) mode, with a pass energy of 200 eV and an energy step of 1 eV for the acquisition of wide-scan spectra, and a pass energy of 50 eV and a step of 0.1 eV for the acquisition of narrow spectra. The spectra obtained were processed using the Avantage software. A Shirley type background subtraction was used and the peak areas were normalized using the Scofield sensitivity factors. The peaks were analyzed using mixed Gaussian-Lorentzian curves (70% of Gaussian character). The binding energies were calibrated against the Csp^3 binding energy set a 284.8 eV. The precision in binding energy is ± 0.2 eV.

The morphology of the dried solid samples was examined using scanning electron microscopy (SEM, HITACHI S3400N, Ltd., Tokyo, Japan) and transmission electron microscopy (Microscope JEM-2100 Plus, 200 kV, JEOL Ltd., Tokyo, Japan).

The thermal stability and composition analysis of the solid samples were performed on a thermogravimetric analyzer using TGA Q500 (TA instruments, USA) under an oxygen flow rate of 60 mL min^{-1}. A weight ranging from 1 to 5 mg of the sample were analyzed. The analysis was carried out using a High resolution mode (Resolution number of 4 and sensitivity value of 1) and the temperature ranged from 22°C to 900°C at an initial heating ramp of 10°C min^{-1}.

Cyclic voltammetry (CV) measurements were carried out using a potentiostatic (MetrOhm Autolab, Netherlands). The electrochemical experiments were conducted using a conventional three-electrode cell setup, featuring an Ag/AgCl reference electrode, a platinum counter electrode, and a glassy carbon (GC) working electrode with a diameter of 3 mm and a surface area of 0.07 cm^2. Prior to use, the working electrodes underwent polishing with SiC-paper and thorough rinsing with ultrapure water. Subsequently, the samples were prepared by combining 180 µL of each irradiated or non-irradiated aqueous solution (GO or rGO) with 20 µL of Nafion as a binder. A 10 µL aliquot of the prepared samples was drop-casted onto the GC working electrode and allowed to dry gradually under ambient conditions. The electrochemical measurements were executed in a 1 M KOH aqueous electrolyte, encompassing a voltage range from -0.2 V to +0.6 V at various scan rates.

2.6 Solubilization tests of rGO

The solubility of rGO powders prepared at 50 kGy (rGO-50 kGy) and dried after centrifugation was systematically evaluated in eighteen different solvents. Each test involved the preparation of rGO suspensions at a concentration of 0.2 g L^{-1}.

Subsequently, the mixtures underwent thorough dispersion using an ultrasonic bath for 2 hours at room temperature. The resulting dispersions were subjected to centrifugation at 4200 rpm for 10 minutes to assess the extent of solubility in the various solvents.

3. Results and discussions

3.1 Radiation induced synthesis of rGO

In the conducted experiments, a 0.2 g L^{-1} aqueous suspension of GO was irradiated with a γ-source at varying doses from 0 to 50 kGy, in the presence of 0.2 mol L^{-1} IPA. Initial visual analysis provided substantial information on the reduction process of GO, as influenced by radiation dose, as can be seen in **Figure 2a**. The GO suspension presented before irradiation a brownish-yellow color which gradually shifted at lower absorbed doses to an opaque black as the dose increased, aligning with findings reported in the literature.[61] A notable change in the suspension's appearance was observed at the threshold dose of

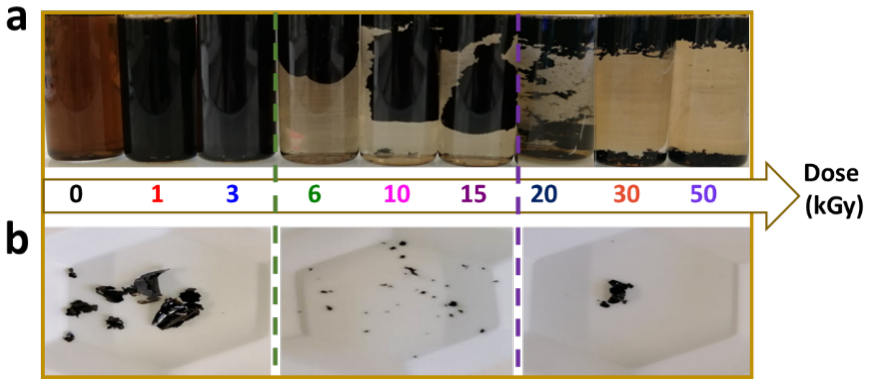

Figure 2. Photographs of GO suspensions with increasing doses from 0 to 50 kGy: **(a)** in aqueous medium without agitation and **(b)** rGO powders obtained via centrifugation (8000 rpm, 30 min) followed by drying (at 100°C; overnight).

6 kGy, marking the stage where the previously homogeneous solution began to form less dense, black hydrophobic agglomerates on the surface of each sample. This behavior is significant, as GO sheets feature oxygen-containing groups such as epoxy, carboxyl, and hydroxyl, which make them hydrophilic through hydrogen bonding and ensure their stable dispersion in water. The radiation-induced reduction of GO should have led to the loss of these groups, fostering hydrophobic interactions primarily via aromatic rings, resulting in the observed agglomeration. These black agglomerates, which should reflect the presence of reduced graphene oxide (rGO), further solidified into sediments at the bottom of the containers with increasing absorbed dose, leaving a supernatant enriched with unreduced GO. Moreover, centrifugation of the irradiated samples yielded a distinct transition in the obtained solid products: from thin layers at doses up to 3 kGy to bulkier flakes at higher doses, particularly after 15 kGy, as illustrated in **Figure 2b**. Smartphone-based imaging was utilized for capturing the varied visual states of rGO across different absorbed doses, providing a clear representation of the changes occurring in the physical attributes and morphology of the rGO attributable to the extent of irradiation and its interaction with the GO material's structure.

3.2 UV-Vis characterization

UV-visible absorption spectroscopy provided insights complementing our visual observations, as demonstrated in **Figure 3a**. Two key absorption bands were discerned in the spectrum of GO before irradiation: a broad band around 230 nm and another at approximately 295 nm. The 230 nm absorption band is attributed to π→π* transitions within aromatic C=C bonds, indicative of the graphitic structure, and the 295 nm band corresponds to n→π* transitions characteristic of carbonyl C=O groups.[62,63] Following radiolytic reduction, a red-shift to higher wavelengths was observed in the π→π* absorption band, up to 35 nm from 6 kGy, suggesting the transition in carbon hybridization in GO from a sp^3 hybridized state, attached to oxygen, to a sp^2 hybridized configuration, thereby regaining the π-conjugation within the GO structure as previously documented.[64]

Above certain radiolytic doses, the spectral profile stabilized, suggesting a saturation point in the GO reduction process, as illustrated in **Figure 3b**. Quantitative analysis determined that a minimum dose of about 6 kGy is necessary to achieve this effect. This threshold was inferred through an exponential fitting approach where the point of convergence between tangent and asymptotic lines on the absorption curve was identified.

A progressive decline in the intensity of the carbonyl absorption band at 295 nm was observed concurrently with the red shift, reaffirming rGO reduction process. This decay in C=O band intensity was systematically related to absorbed dose, elucidating a thorough alteration of carbonyl functionalities as evidenced in **Figure 3c**. From the exponential fitting of this decay (first-order decay) and by using equation (3), one can deduce the initial yield of consumption of carbonyl groups, which can be in first approximation related to the initial yield of radiation induced reduction of GO (G_{red}).

To provide more detail, the initial reduction yield of graphene (G_{red}) was defined as follows:

$$G_{red} = \frac{1}{d}\left(\frac{d\,[GO]}{d\,D}\right)_0 \qquad \textbf{Eq.6}$$

where [GO] represents GO concentration, D the absorbed dose and d the solution density (1 kg/L).

Subsequently, we engaged the Beer-Lambert's law to compute G_{red}:

$$G_{red} = \frac{1}{\varepsilon_{295} \times l \times d}\left(\frac{d\,A_{295}}{d\,D}\right)_0 \qquad \textbf{Eq.7}$$

where ε_{295} is the molar extinction coefficient at 295 nm, l is the path length (0.2 cm) and $\left(\frac{d\,A_{295}}{d\,D}\right)_0$ is the initial slope of the absorbance at 295 nm versus the absorbed dose as deduced from **Figure 3c**.

Using Beer-Lambert's law, we found ε_{295} to be 23.3 g^{-1} L mol^{-1} cm^{-1} (**Figure S1** in ESI). As a consequence, according to equation (7), GO reduction yield was found to be: $G_{red} = 3.3 \times 10^{-5}$ g J^{-1}. This value, never evaluated in literature but recorded here for the first time, was found independent of the initial GO

concentration (for 0.1, 1, and 2 g L^{-1} in GO) (results not presented in the present paper). One can then wonder whether both e_{aq}^- and (CH3)2C•OH are involved in GO reduction. However, direct comparison of GO reduction yield (G_{red}= 3.3 × 10^{-5} g J^{-1}) with the yields of production of reducing species ($G(e_{aq}^-)$ = 2.8 × 10^{-7} mol J^{-1} and $G((CH_3)_2C^{\bullet}OH)$= 3.4 × 10^{-7} mol J^{-1} or eventually with the maximal yield of reduction ($G_{red_{max}}$ = $G(e_{aq}^-)$ + $G((CH_3)_2C^{\bullet}OH)$ = 6.2×10^{-7} mol J^{-1}) is unfeasible due to the lack of precise molar mass for GO.

Nevertheless, with the aim to ascertain the involvement of isopropanol radicals ($(CH_3)_2C^{\bullet}OH$) in GO reduction mechanism, similar irradiation experiments were conducted using tert-butanol (*t*-BuOH) instead of isopropanol under analogous conditions (ESI, **Figures S2 and S3**). The results, pertaining to UV-visible spectra, suggested a more pronounced GO reduction in the presence of IPA, whicl conjugation and the nigh disappearance of the n→π* transition corresponding to C=O groups. The absorbed dose which is necessary for the reduction of 0.2 g L^{-1} in GO in presence of *t*-BuOH was found to be 11 kGy, notably higher than the 6 kGy required in presence of IPA, underscoring the superior reducing capability of IPA radicals over *t*-BuOH radicals.

The difference between IPA radical and t-BuOH radical reactivities, was quantitatively supported by the reduction yield of GO found in the presence of *t*-BuOH: 1.9 × 10^{-5} g J^{-1}, which is approximately 1.7 times lower than the yield found in the presence of IPA (3.3 × 10^{-5} g J^{-1}). This ratio is not far from that obtained by dividing $G_{red_{max}}$ (= $G(e_{aq}^-)$ + G((CH3)2C•OH)) by $G(e_{aq}^-)$, which amounts to 2.2. This implies that in presence of *t*-BuOH only e_{aq}^- react on GO, while in presence of IPA, in addition to e_{aq}^-, most of isopropanol radicals also reduce GO into rGO.

3.3 Raman spectroscopy analysis

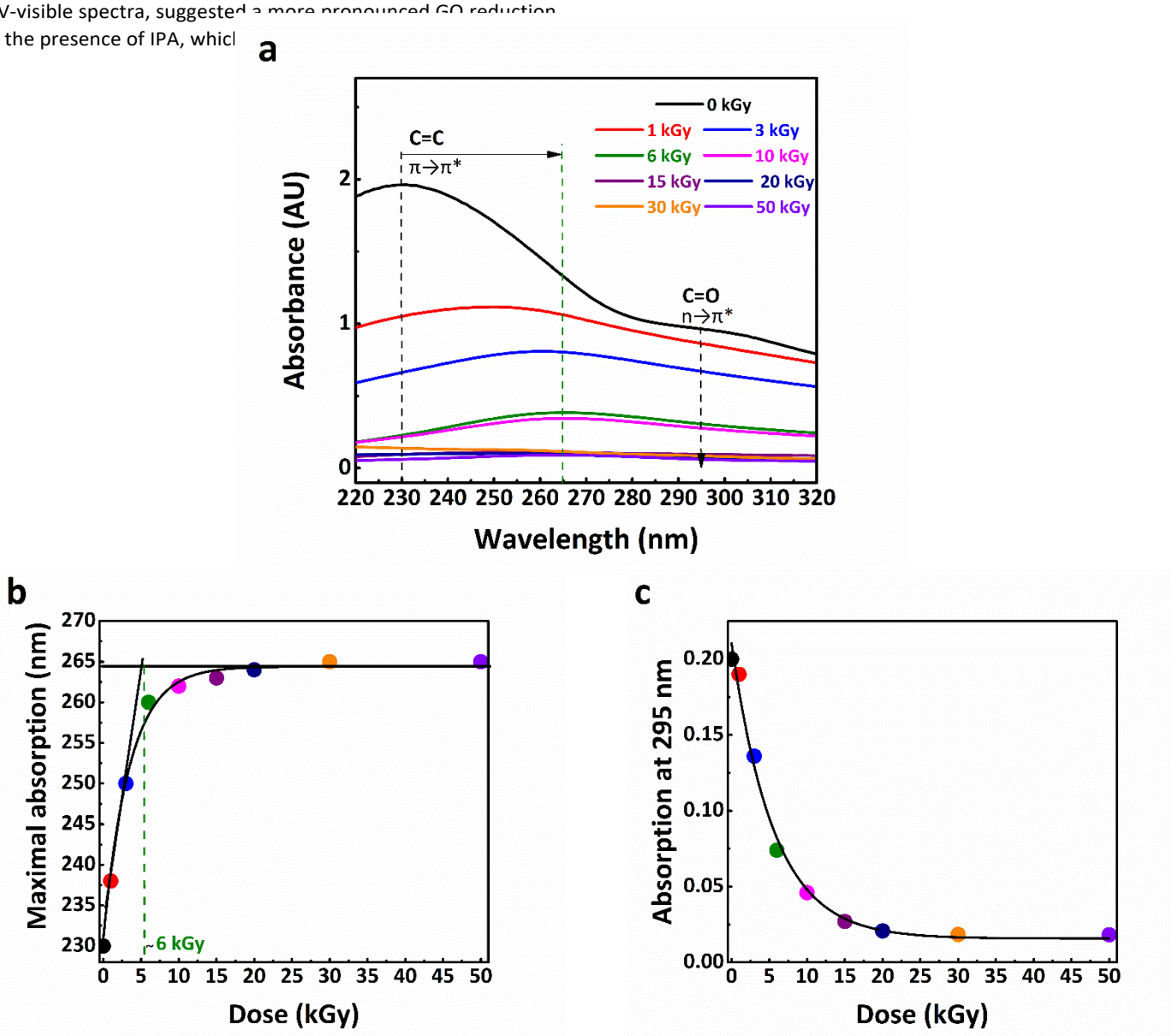

Figure 3 (a) UV-visible absorption spectra of an aqueous suspensions of GO (0.2 g L^{-1}), illustrating the impact of absorbed doses ranging from 0 to 50 kGy, with an optical path length of 0.2 cm and pure water serving as reference, **(b)** Exponential curve fitting of the variation of maximal absorption as a function of absorbed dose, representing the extent of sp^2 hybridization; **(c)** Exponential curve fitting of the decay of C=O absorption band at 295 nm as a function of absorbed dose.

In this study, Raman spectroscopy, a non-destructive analytical tool commonly used to investigate carbon-related materials, was deployed to confirm the reduction of the samples and evaluate structural changes in the commercial GO following radiolytic reduction under ambient conditions.[65] The analysis of main Raman peaks, including D, G, 2D and D+D', plays a crucial role in understanding the structural characteristics of the graphene material. Additionally, the relative intensity ratio ID/IG is highlighted as an important parameter, with an increase in ID/IG reflecting a reduction in the oxidation level. The D band is related to defects or lattice disorder due to oxygen-functional group binding.[66] The G band, on the other hand, corresponds to sp2 hybridized carbon-based material.[66] The 2D band is the second order of the D band. Just like the D band, the D + D' band is associated with the number of defects and disorder.[67] The prominence of D and G bands in graphene-based materials generally reflects the disorder level associated with sp^3 defects, edge imperfections, or amorphous carbon residuals, wherein alterations in their relative intensities in Raman spectra can manifest the extent of GO reduction.[68,69] It is noted in the literature that the ID/IG ratio used for identifying GO and rGO in Raman spectroscopy falls within wide ranges of 0.67–1.4 and 0.91–1.9,[70–72] respectively (see also **Table 1**), presenting a challenge for the comparison of graphene materials. This variability is attributed to factors such as laser wavelength, intensity, and the approach of single point measurement spectra, all of which could introduce additional uncertainty in the ID/IG peak intensity ratio.[72,73]

Figure 4a displays the Raman spectrum of non-irradiated GO (black plot) as well as the spectra of irradiated GO solutions. Non-irradiated GO spectrum highlights the four distinguishable bands: D, G, 2D, and D+D' located at vibrational frequencies of 1353 cm^{-1}, 1601 cm^{-1}, 2694 cm^{-1}, and 2935 cm^{-1}, respectively. An observed downshift by 11 cm^{-1} and 7 cm^{-1} in the D and G bands of GO, respectively, with increasing absorbed doses from 0 to 6 kGy, is indicative of strain induced in the graphene sheets during the reduction process,[74] confirming the successful reduction of 0.2g L^{-1} of GO starting from 6 kGy. The subsequent analysis of radiolytically rGO in **Figure 4b** reveals notable changes, particularly an increase in the ID/IG ratio from 0.99 to 1.40 with increasing absorbed dose from 0 to 50 kGy. This rise indicates that radiation-induced reduction alters the structure of GO, resulting in the generation of defects and a higher degree of recovery of sp2 domains in rGO. These findings are consistent with previous documented results,[75,76] supporting the efficient restoration of π-conjugation in rGO following radiolytic reduction. Moreover, the higher ID/IG ratios of rGO at high absorbed doses compared to those obtained by other reduction methods may be attributed to the extensive formation of new smaller sp^2-hybridized domains induced by γ-ray irradiation. A noteworthy finding was that the 2D and D+D' bands exhibited no significant alterations pre- and post- γ-irradiation, indicating that the structural multiplicity of reduced graphene remains unaffected, contrary to the patterns observable in self assembled rGO layers,[77] which will be further discussed in the electron microscopy section.

Table 1. Comparison of the ID/IG ratios of GO and rGO obtained using different reduction methods reported in the literature and using our radiolytic method.

Reduction Method	ID/IG for GO	ID/IG for rGO	Reference
Chemical	0.89	1.68	16
	0.91	1.20	75
	0.97	1.40	76
	1.10	1.30	78
Thermal	1.36	1.87	79
	1.05	1.03	17
Electron beam	1.05	1.23	17
Gamma irradiation	1.05	1.21	17
	1.03	1.53	41
	1.02	1.24	50
	0.70	0.83	49
	0.91	1.21	48
	0.99	1.40	Our study

3.4 ATR-FTIR spectroscopy analysis

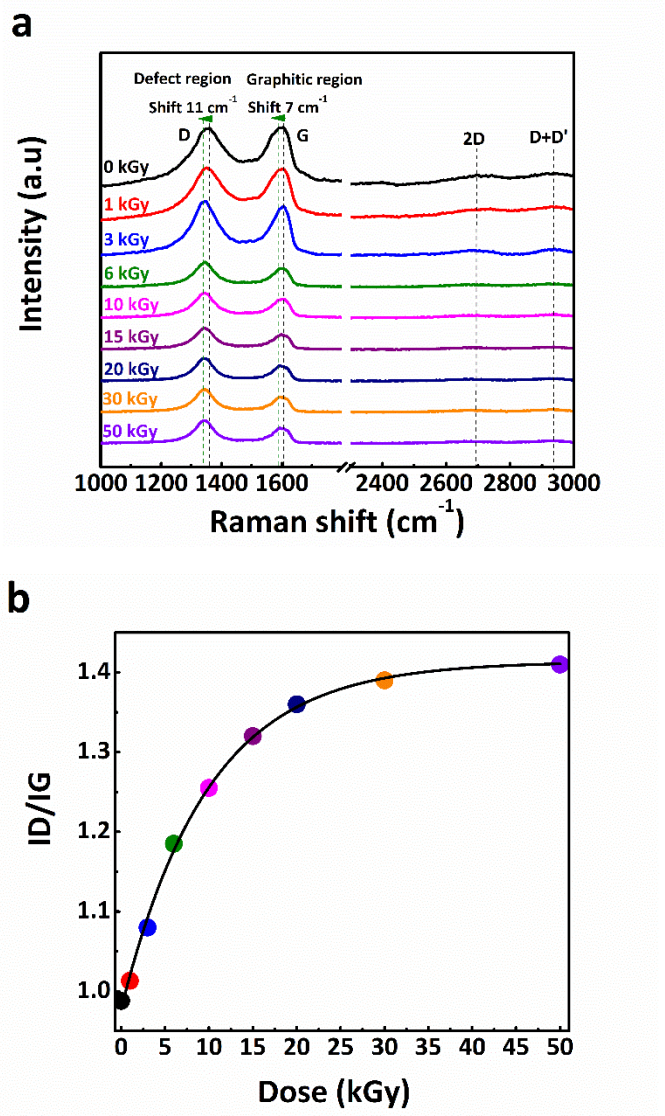

Figure 4 (a) Raman spectra of GO before and after γ- irradiation at increasing doses, **(b)** Exponential curve fitting of the variation of D/G ratio (determined from the positions at 1343 cm^{-1} and 1594 cm^{-1} for the D and G bands) as a function of absorbed dose.

The ATR-FTIR analysis serves as a critical tool in elucidating the presence of oxygen functional groups in graphene oxide (GO), which is crucial for validating the radiolytical reduction process in our samples.

As illustrated in **Figure 5**, the ATR-FTIR spectral analysis depicts the characteristic oxygen-containing functionalities associated with sp^3-hybridized carbon in GO sheets. A broad transmittance band ranging approximately from 3700 to 3000 cm^{-1} highlights the presence of hydroxyl and carboxylic groups (-OH). Additionally, vibrational signatures at 1718 cm^{-1} (C=O), 1440 cm^{-1} (C-OH), 1224.8 cm^{-1} and 1057 cm^{-1} (C-O) delineate the various oxygenated-functionalities on GO, such as carboxylic, hydroxyl, and epoxy groups.[80,81] Peaks observed at 2940, 1620, and 1410 cm^{-1} can be ascribed to C-H stretching, C=C stretching, and C-H bending modes respectively, confirming the analytical purity of the commercial GO suspension before γ-irradiation.

Upon exposure to γ-rays, the FTIR spectra exhibited significant changes, particularly in the attenuated intensities of peaks linked to oxygenated groups (e.g., C=O, C-O, and C-O-C), with a pronounced disappearance after a 6 kGy absorbed dose.

However, the C=C band intensity remained largely unaffected even at the maximum applied dose (50 kGy), clearly denoting sp^2 hybridization restoration within the graphene sheet through radiolysis of the aqueous GO suspension, culminating in the synthesis of rGO. It is important to note that the residual -OH stretching mode persisted across all rGO samples, irrespective of the radiation dose, confirming the remaining of hydroxyl groups even after a high-dose radiolytic treatment.[82]

3.5 XPS analysis

The confirmation of rGO formation was further solidified through XPS analysis, with the results depicted in **Figures 6 a-f**. Notably, the survey spectrum showcased in **Figure 6a**, confirmed rGO's high purity, displaying only the characteristic C1s and O1s peaks. This absence of additional peaks categorically excludes impurities, addressing potential concerns regarding extrinsic element contamination, which is notably prevalent in various chemical reduction processes described in previous studie.[83,84] Prior to reduction, the spectrum for GO is defined by a pronounced O1s peak, indicative of abundant oxygen-containing groups. After subjecting GO to γ-irradiation, a discernible diminution of the O1s peak, proportional to radiation dosage, was observed in the rGO sample, strongly suggesting the effective removal of oxygen functional groups during the reduction process.

The calculated C/O ratio in terms of relative atomic percentages was found to be 3.3 and 11.1 for GO and rGO, respectively, indicating the highly effective deoxygenation of GO through our radiolytic reduction methodology as compared to other methods (**Table.2**). The evolution of the C/O ratio is depicted in **Figure 6b**, illustrating a significant increase with increasing absorbed dose from 0 to 50 kGy. Notably, the point of intersection between the tangent line drawn on the exponentially fitted curve and the asymptote confirms that the theoretical absorbed dose for the radiolytic reduction of GO is about 6 kGy. These results are in strong agreement with the findings discussed earlier.

The C1s core-level XPS spectra of non-irradiated GO as well as the spectra of irradiated GO (irradiated at 6 and 50 kGy) are portrayed in **Figure 6c** and further deconvoluted in **Figures 6 d-f**, respectively. The C1s XPS spectra of GO (**Figure 6d**) exhibited a peak at 284.8 eV corresponding to C-C bonds of carbon atoms in a conjugated honeycomb lattice, alongside three distinct peaks centered at 286.8 eV, 287.2 eV, and 288.6 eV, attributable to single or double bonds in aromatic rings, i.e. C-O (epoxy and alkoxy), C=O, and O-C=O groups, respectively, which are consistent with the previous reports.[41,85]

Transitioning through radiolytic reduction, a noticeable attenuation of oxygen-related peaks was observed, (**Figures 6 c-f**), emphasizing the eradication of oxygen functional groups in rGO during γ-ray irradiation. However, residual functional groups at the edges of GO sheets remained at an absorbed dose of 50 kGy.

Complementarily, the strengthened C=C bond peak at 284.6 eV and the emergence of the π-π* shake-up peak with progressive doses reflect the reconstitution of the sp^2 carbon lattice, a finding that echoes previously established literature[41] and reaffirms our earlier discussions. Moreover, the left peak assigned to the C-C bond was shifted to a lower binding energy by approximately 0.2 eV, further confirming the transition to C=C characteristics, as shown in **Figure 6c**. The peak at 284.6 eV, dominated by sp^3 carbon, remains prevalent throughout the carbon skeleton. The XPS analysis effectively validates the transition from GO to rGO, emphasizing the removal of oxygen-containing functional groups and the restoration of the sp^2 carbon network, providing crucial insights into the chemical and structural transformations during the radiolytic reduction process.[86]

Table 2. Comparison of the C/O ratios of GO and rGO obtained using different reduction methods reported in the literature and using our radiolytic method.

Reduction Method	C/O ratio for GO	C/O ratio for rGO	Reference
Chemical	2.0	9.5	[16]
	2.4	7.1	[87]
	2.2	5.9	[83]
	2.3	9.1	[84]
	1.6	3.0	[17]
Thermal	2.3	5.1	[19]
	2.4	6.5	[18]
	1.6	6.2	[17]
Electron beam	1.6	5.4	[17]
Hydrothermal	1.6	7.9	[88]
Gamma irradiation	1.1	10.1	[41]
	2.9	6.5	[49]
	2.6	5.0	[48]
	1.6	4.1	[17]
	3.3	11.1	Our study

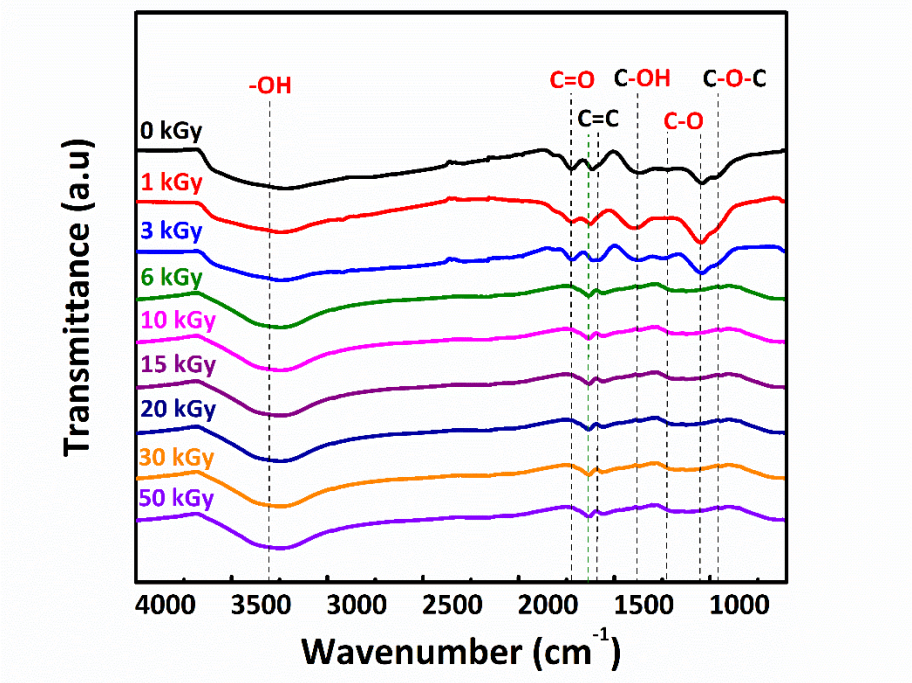

Figure 5 FT R spectra of GO before and after γ-irradiation at increasing absorbed doses from 0 kGy to 50 kGy.

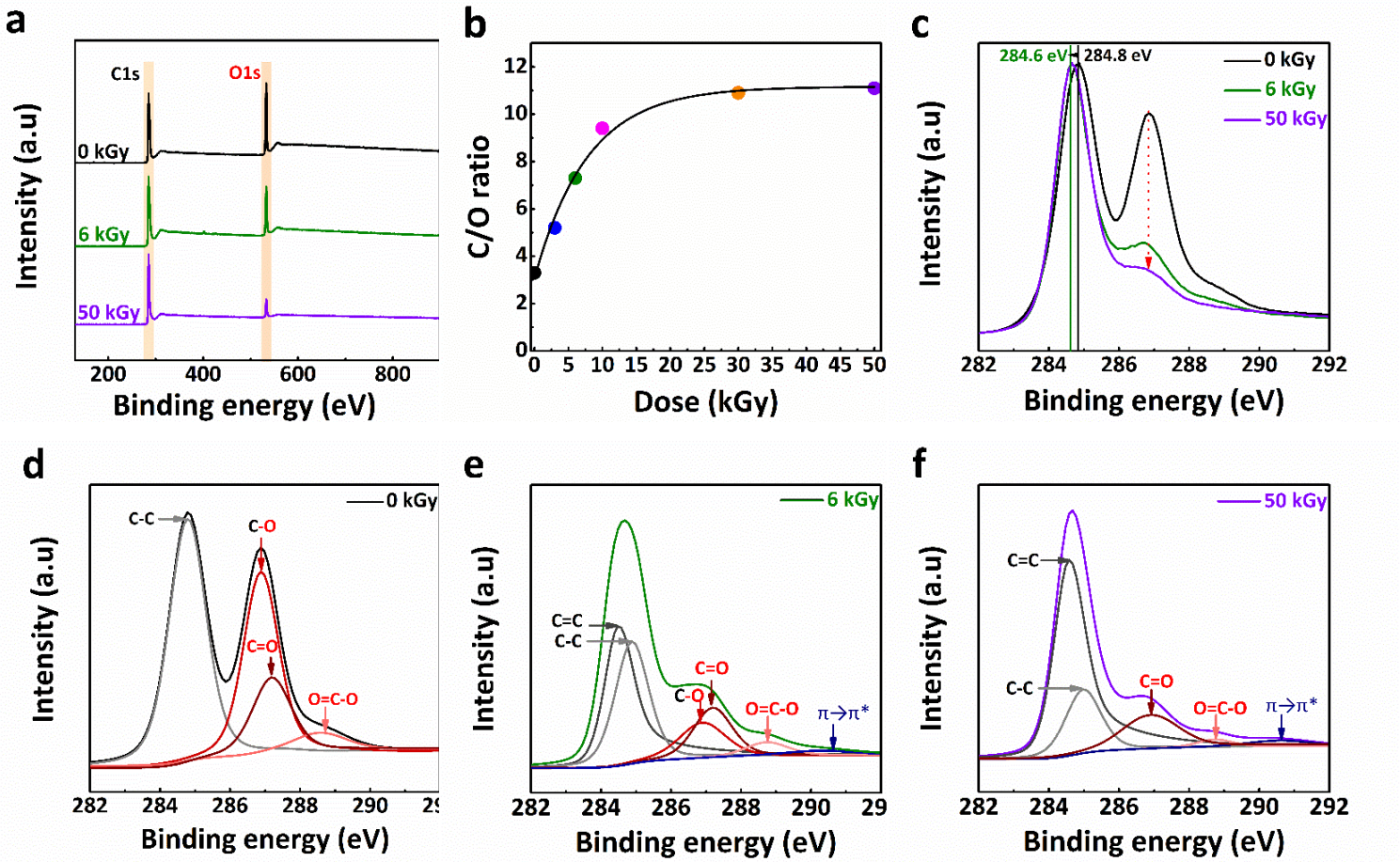

Figure 6. (a) XPS sur ey spectra of GO (b ack p ot) and rGO rad ated at 6 kGy (green p ot) and 50 kGy (o et p ot). **(b)** Exponent a cur e f t ng of the variation of C/O ratio as a function of absorbed dose. **(c)** Reduct on of oxygenated funct ona groups n GO (b ack p ot) w th ncreas ng absorbed doses (6 kGy (green p ot) and 50 kGy (o et plot).. XPS spectra of C1s for GO before and after rad at on at **(d)** 0 kGy, **(e)** 6 kGy, and **(f)** 50 kGy.

3.6 Structural and morphological characterizations

In the pursuit of comprehensive characterization, SEM and EDX were employed to respectively study the variation in morphology and in elemental composition of the samples with increasing the absorbed dose.

Figure 7a exhibits distinctive features of a typical wrinkled structure and folded flat surfaces of GO, indicative of its thin and smooth layering.[89] Upon performing radiolysis, the layers became more discernible, with a reduction in oxygenated functional groups becoming apparent, particularly notable at 6 kGy, where the features displayed smaller dimensions and folded wrinkles. This effect was further accentuated at the maximal absorbed dose of 50 kGy, as illustrated in **Figure 7a**, resulting in a highly disordered, aggregated, and fully inflated structure in the carbon skeleton[90,91], consistent with the Raman data. This transformation aligns with the removal of oxygenated functional groups, leading to a reduction in the distance between layers of the GO and the subsequent self-assembly of graphene layers. The aggregation of rGO at higher absorbed doses may be attributed to factors such as reduced solubility, interlayer interactions, covalent bond formation, morphological changes induced by radiation, and the formation of byproducts. These elements lead to the observed aggregation, contrasting with the typical structure of non-irradiated GO.

SEM micrographs in the ESI, **Figure S4**, further support this visual progression with additional evidence of structural changes.

Furthermore, to substantiate these findings, TEM images of the aqueous suspensions were examined, confirming the thin-layered structures of both GO and reduced graphene oxide (rGO), as depicted in **Figure S5**, in agreement with prior studies.[92,93] To affirm the chemical compositions and purity of rGO, EDX was carried out over various locations of the different irradiated and non-irradiated samples. The spectra revealed the presence of both carbon and oxygen elements within the graphene sheet. By evaluating the C/O ratio, the extent of reduction was quantified. The calculated C/O ratio increased from 3.3 for non-irradiated GO to 11.2 for rGO obtained at the highest absorbed dose (50 kGy), as depicted in **Figure 7b**. These results are in excellent agreement with the XPS findings detailed in the previous section. This significant increase in C/O ratio (3.4 times higher in case of rGO) highlights the effective aromatization in the graphene sheet together with the consumption of oxygenated functionalities initially present in GO through radiolytic processes. It is worth noting that to the best of our knowledge, this C/O ratio surpasses those achieved through other reduction methods as proposed in the existing literature.[16–18]

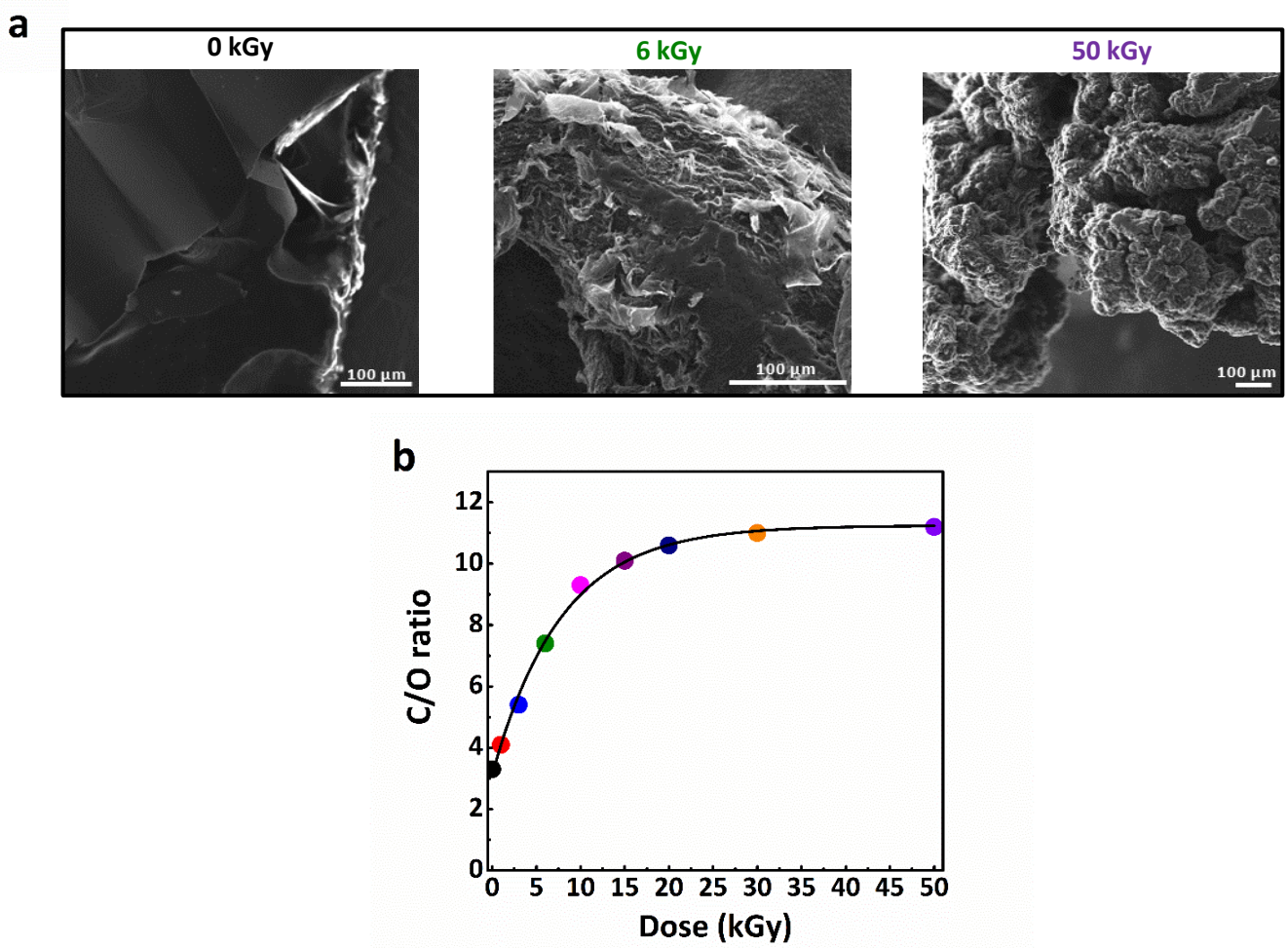

Figure 7. (a) SEM images of GO before and after γ-irradiation (scale bar: 100 µm), and **(b)** Exponential curve fitting of the variation of C/O ratio (obtained by EDX experiments) as a function of absorbed dose.

3.7 Thermogravimetric analysis (TGA)

Given the success of the radiolytic route in synthesizing rGO, it became imperative to investigate the thermal stability of the obtained materials. TGA not only serves as a potent tool for examining the thermal stability of various samples but also for validating the efficiency of reduction processes. [94]

The mass loss of non-irradiated GO (depicted in black, 0 kGy) and those of irradiated samples (represented in green, 6 kGy, and violet, 50 kGy) were plotted against temperature, as depicted in **Figure 8**.

The TGA plot of GO unveils three distinct stages of weight loss. Initially, in the first stage, the elimination of low-boiling solvents, including moisture, occurred below 100°C. Subsequently, at mid-range temperatures, mass loss was attributed to the decomposition of oxygenated groups such as epoxy, hydroxyl, carboxyl, anhydride, or lactone groups, in agreement with reported literature.[95] The final stage of mass loss (400 - 600°C) corresponds to the final decomposition of the carbon skeleton.

Consistent observations were made for the samples irradiated at 6 kGy and 50 kGy. Significantly, the radiation-induced synthesis of rGO demonstrated superior thermal stability of rGO as compared to that of GO. Indeed, in case of non-irradiated GO, a weight loss of 27% was observed in the temperature range of 160-280°C. This weight loss decreased to 15% and 10% in case of rGO prepared upon 6 kGy and 50 kGy irradiation, respectively. This substantial increase in thermal stability highlights the successful synthesis of rGO via radiolytic reduction of GO, corroborating existing literature.[95]

3.8 Cyclic voltammetry (CV) analysis

As demonstrated in our work, radiolytic reduction of GO has led to enhanced aromatization and, by inference, should have improved electrical conductivity of graphene-based materials. Keen to delve into the intrinsic electrochemical characteristics of our materials, we engaged CV experiments to detail their capacitive responses.

Using a three-electrode cell immersed in 1 M KOH aqueous electrolyte, we recorded the cyclic voltammograms of irradiated and non-irradiated samples, over a series of scan rates from 10 to 100 mV s^{-1}. The potential window was carefully selected from 0 to 0.8 V (referenced to Ag/AgCl) to preclude any faradaic processes throughout the experiments.

The obtained cyclic voltammograms, represented in **Figures 9 a-c**, show a direct proportionality of the current intensity to the scan rate, indicating a behavior consistent with capacitive currents. Notably, rGO synthesized at higher absorbed doses, particularly from 6 to 50 kGy, exhibited nearly rectangular cyclic voltammograms at a scan rate of 100 mV s^{-1}, a stark contrast to non-irradiated GO and a characteristic indicative of ideal supercapacitive behavior (**Figure 9d**).

To quantify this performance, we calculated the specific capacitance (C) of the materials from the CV curves using the general equation:

$$C = \frac{\int_{E_1}^{E_2} idV}{\Delta V \times m \times v} \qquad \textbf{Eq.8}$$

Here, C represents the specific capacitance in F g^{-1}, "i" signifies the positive/negative scan current (A), "V" denotes the corresponding voltage (V), ΔV represents the potential window in volts, "m" indicates the active material mass in grams, and " v " is the scan rate in mV s^{-1}.

The rGOs materials prepared at 6 kGy and 50 kGy demonstrated specific capacitances of 124 F g^{-1} and 229 F g^{-1} at 100 mV s^{-1}, respectively, very much higher than that obtained in case of non-irradiated GO, which amounted to only 15 F g^{-1} at the same scan rate (**Figure 9 e**). This clearly demonstrates that the rGO synthesized using our radiolytic method can achieve a specific capacitance up to fifteen times greater than that of GO before irradiation. It is well-known that the capacitance performance of carbon materials is heavily reliant on their specific surface area and pore size. In this context, structural defects and surface chemistry, including the nature and amount of oxygen groups, play a crucial role in improving the capacitive performance of carbon materials.[96] Defects, heteroatom doping, and residual oxygen alter the electro-neutrality of graphene, facilitating easy access of ions and electrolytes to the electrode. This, in turn, leads to increased pseudocapacitance, high charge storage capacity, and rapid charge-discharge rates.

In comparison to literature, rGO obtained through chemical reduction with hydrazine hydrate illustrated a specific capacitance of 135 F g^{-1} in 5.5 M KOH [97] and 49.9 F g^{-1} in 1.5 M KOH [98]. Similarly, reductions with hydrobromic acid resulted in capacitances of 348 F g^{-1} and 158 F g^{-1} in 1M H_2SO_4 and $BMIPF_6$, respectively,[99] while using ascorbic acid produced values of 137.4 F g^{-1} at 10 mV s^{-1} and 41.3 F g^{-1} at 100 mV s^{-1}, in 6 M KOH.[100] Electrochemically reduced GO and flame-reduced GO showcased capacitances of 223.6 F g^{-1} (at 5 mV s^{-1} in 1M H_2SO_4), [101] and 212 F g^{-1} (in 2 M KOH),[102] respectively. Hydrothermally reduced GO and thermally exfoliated rGO both presented lower specific capacitances of 139 F g^{-1} (in 1 M KOH)[103] and 117 F g^{-1} (in H_2SO_4) [104], correspondingly.

The variability in the obtained capacitance values agrees with the understanding that the method of GO reduction influences factors such as morphology, oxygen functional group concentration, and the presence of defects and impurities within the rGO sheets. Additionally, the choice of electrolyte significantly impacts specific capacitance measurements, as observed in comparison between aqueous (acidic or alkaline) and organic electrolytes, KOH being often favored due to its non-toxicity, cost-effectiveness, and excellent conductivity.[105] Parameters such as electrolyte concentration and scan rate further modulate specific capacitance values.[98]

In light of this analysis, our radiolytically prepared rGO emerges as an exceptional candidate for supercapacitor applications, demonstrating outstanding specific capacitance when benchmarked against reported values in the field.

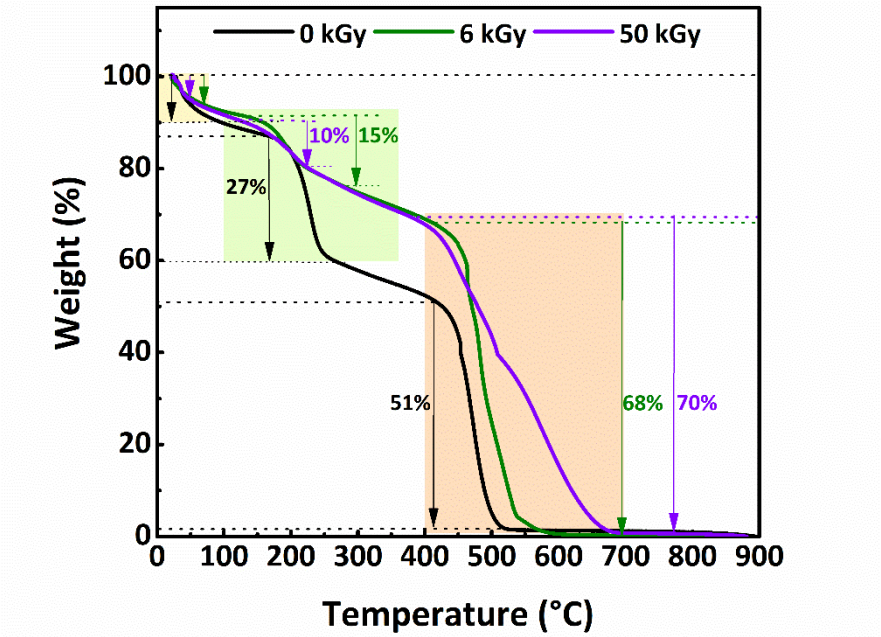

Figure 8. Thermogravimetric analysis of non irradiated GO (black plot) and irradiated GO at 6 kGy (green plot) and 50 kGy (violet plot)

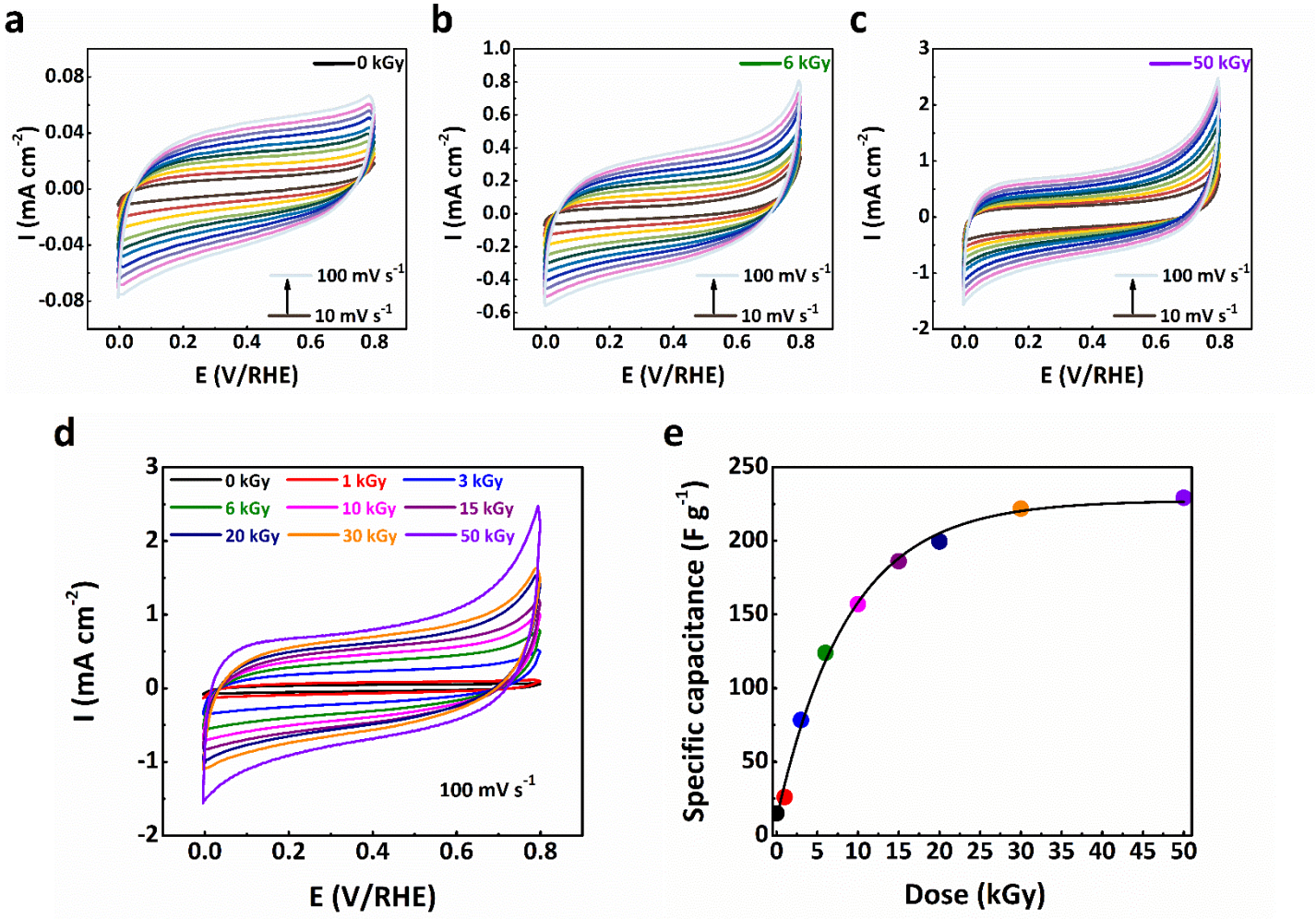

Figure 9. Cyclic voltammograms of graphene oxide acquired at various scan rates (10-100 mV s^{-1} after each increment of 10 mV s^{-1}) **(a)** 0 kGy, **(b)** 6 kGy and **(c)** 50 kGy. **(d)** Evolution of CV Curves of GO across absorbed doses ranging from 0 to 50 kGy at a fixed scan rate of 100 mV s^{-1} ; **(e)** Exponential curve fitting of the variation with absorbed dose of specific capacitance value

3.9 Solubility of rGO

Though numerous materials have demonstrated superior properties at the lab scale, their limited solubility often hinders their practical and industrial applications.[106] rGO is also affected by this limitation due to its hydrophobic nature caused by aromaticity and scarcity of hydrophilic functional groups. It is thus imperative to mention that rGO prepared by radiolysis exhibited exceptional solubility without the use of harsh conditions.

A comprehensive assessment involving eighteen different solvents (**Figure 10**) was conducted to showcase this notable property. Specifically, rGO prepared with 50 kGy-irradiation underwent bath-sonication at room temperature for 2 hours and was then left undisturbed to observe the extent of sedimentation. The results revealed the excellent solubility of rGO in DMF (see **Figure.S6** in the ESI), even after 10 minutes of centrifugation at 4200 rpm, while also demonstrating notable stability in environmentally benign solvents such as ethanol. Conversely, poor solubility was observed in aqueous systems, possibly attributable to the mismatch in surface tension between the rGO layers and water. The enhanced solubility in DMF can be ascribed to the solvent's high polarity, surface tension, cohesive energies, and solvation effect on the rGO sheets.[107] It is crucial to acknowledge that while some solvents may share similarities in polarity with DMF or ethanol, their unique solvating abilities and cohesive energies could impact the dispersibility of rGO.

The dispersibility of rGO in various solvents is primarily determined by the surface functionalities of the rGO and Hansen parameters of the solvents.[107] The presence of polar hydroxyl groups and residual oxygen functional groups at the edges of GO sheets, confirmed by FTIR and XPS data, facilitates intermolecular hydrogen bonding with polar solvents, attributing to the enhanced solubility in DMF.

Sonication is widely employed for dispersing rGO into solvents, predominantly by creating shear stresses and cavitation, although extreme conditions have been reported to enable dispersion into poor, low boiling point solvents, albeit with longer sonication times (48 h). However, prolonged sonication times are generally undesired as they can reduce sheet size and introduce defects that undermine rGO's properties.[108]

The critical role of surface tension in solvent selection for graphene and its derivatives cannot be overstated.[109] The presence of oxygen-containing groups in GO results in higher surface energy compared to rGO, where the loss of surface polarity increases its hydrophobicity.

Wettability and contact angle measurements have estimated the surface energies of GO and rGO to be approximately 62 mN m^{-1} and 46 mN m^{-1}, respectively.[110] Solvents with surface tensions similar to these values are the most effective for dispersing GO and rGO.

Further provisional examinations are necessary to verify and explore these findings.

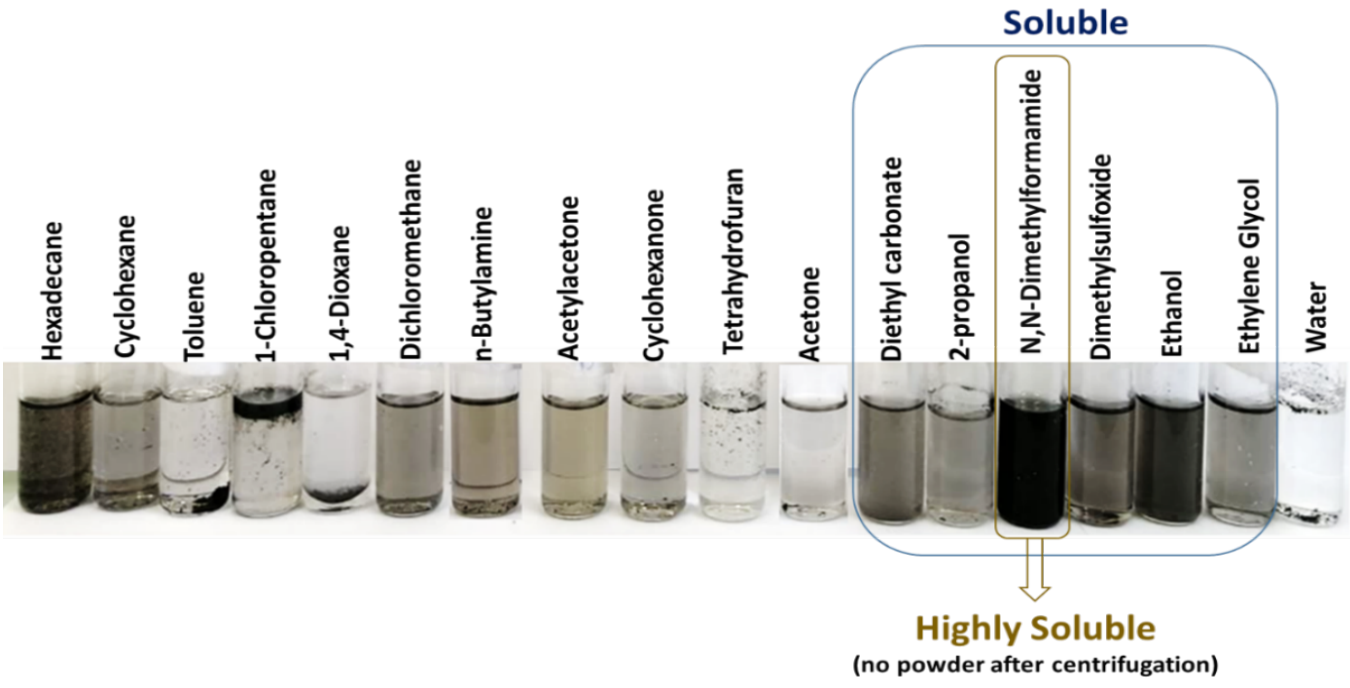

Figure 10. Photographs depicting the solubility of rGO (obtained at an absorbed dose of 50 kGy) in various solvents after ultrasonication for 2 hours at room temperature.

Conclusion

Addressing the need for eco-friendlier and safer rGO production methods, our study harnessed the power of gamma irradiation to reduce commercial GO in an eco-friendly aqueous medium under standard conditions. The process initiates the homogeneous formation of rGO in aqueous solution by generating reducing radicals. We delved into the impact of absorbed dose on GO reduction in deoxygenated aqueous solutions containing isopropanol or tert-butanol, establishing the radiolytic yield of GO reduction as independent of the initial GO concentration but dependent on the used alcohol. The reduction yield of GO in the presence of isopropanol was found to be 3.3×10^{-5} g J^{-1}, approximately 1.7 times higher than the yield observed in the presence of tert-butanol (1.9×10^{-5} g J^{-1}). This insight is particularly valuable for predicting the necessary absorbed dose for a given amount of GO, with a noticeably lower absorbed dose required for IPA compared to *t*-BuOH. Crucially, the reduction process underwent comprehensive scrutiny utilizing advanced instruments and remarkably, it does not necessitate any external agents apart from the radiation source.

The gamma rays effectively reduced 0.2 g L^{-1} of GO across a spectrum of 6 kGy to 50 kGy, each exhibiting unique efficacies. The suite of characterization techniques implemented, including UV-Vis spectroscopy, Raman spectroscopy, ATR-FTIR spectroscopy, XPS, EDX, and TGA, verified the effective elimination of most oxygen-containing groups and the re-establishment of the sp2 carbon lattice indicative of rGO.

Markedly, the rGO synthesized at an absorbed dose of 50 kGy showed superior qualities in comparison to both rGO from this study at lower dosages and those produced through other methodologies, namely:

a. A considerably high C/O ratio exceeding 12,
b. Crystalline purity levels,
c. An I_D/I_G ratio of 1.4,
d. A substantial specific capacitance reaching 229 F g^{-1},
e. Notable thermal stability,
f. And outstanding solubility in DMF.

These encouraging outcomes demonstrate that gamma irradiation stands as a promising, clean, and efficient alternative for fabricating rGO, making it exceptionally suitable for applications like supercapacitors and thermoresistors.

Our team remains committed to the advancement of nanocomposites based on rGO, envisioning the broad adaptation of the radiolytic approach, which could revolutionize multiple industrial sectors.

Author Contributions

Souad Abou Zeid: Methodology, Formal analysis, Investigation, Conceptualization, Software, Validation, Resources, Writing-original draft, Writing-review and editing, Visualization. **Selma Bencherif**: Formal analysis, Investigation (CV experiments). **Rasta Ghasemi**: Validation, Investigation (SEM and EDX experiments). **Rituporn Gogoi**: Formal analysis. **Yamina Chouli**: Formal analysis. **Matthieu Gervais**: Validation, Investigation (TGA experiments). **Diana Dragoe**: Validation, Investigation (XPS experiments). **Jalal Ghilane**: Validation, Investigation (CV experiments). **Prem Felix Siril**: Visualization, Formal analysis, Investigation (Raman experiments). **Samy Remita**: Conceptualization, Methodology, Validation, Writing - original draft, Writing - review and editing, Visualization, Supervision, Project administration.

Acknowledgements

The first author extends heartfelt appreciation to Dr. Wafaa Noun of the Faculty of Science (Branch 1), Lebanese University, Lebanon, for her invaluable support and guidance throughout the course of this research. The authors are also grateful to François Brisset of ICMMO, UMR 8182, CNRS, Université Paris-Saclay, France, for conducting TEM experiments, which greatly contributed to the advancement of this study. Additionally, the authors acknowledge the curators of the Franco-Indian SPARC (Scheme for Promotion of Academic and Research Collaboration) project for their support and collaboration.

Conflicts of interest

There are no conflicts to declare. The authors declare that they have no known competing financial interests or personal relationships that could have appeared to influence the work reported in this paper.

References

1 A. K. Geim, *Science*, 2009, **324**, 1530–1534.

2 A. K. Geim and K. S. Novoselov, *Nat. Mater.*, 2007, **6**, 183–191.

3 M. Czerniak-Reczulska, A. Niedzielska and A. Jędrzejczak, *Adv. Mater. Sci.*, 2015, **15**, 67–81.

4 M. C. Lemme, T. Echtermeyer, M. Baus, B. N. Szafranek, M. Schmidt and H. Kurz, *ECS Trans.*, 2007, **11**, 413–419.

5 R. Forsyth, A. Devadoss and O. J. Guy, *Diagnostics*, 2017, **7**, 45.

6 K. R. Amin and A. Bid, *ACS Appl. Mater. Interfaces*, 2015, **7**, 19825–19830.

7 R. Zhang, X. Yu, Q. Yang, G. Cui and Z. Li, *Constr. Build. Mater.*, 2021, **294**, 123613.

8 A. S. Vorobev, G. V Bianco, G. Bruno, A. D'Orazio, L. O'Faolain and M. Grande, *Appl. Sci.*, 2021, **11**, 8367.

9 X.-Y. Yan, X.-L. Tong, Y.-F. Zhang, X.-D. Han, Y.-Y. Wang, G.-Q. Jin, Y. Qin and X.-Y. Guo, *Chem. Commun.*, 2012, **48**, 1892–1894.

10 G. M. da Costa and C. M. Hussain, *Compr. Anal. Chem.*, 2020, **91**, 263–279.

11 K. S. Novoselov, A. K. Geim, S. V Morozov, D. Jiang, Y. Zhang, S. V Dubonos, I. V Grigorieva and A. A. Firsov, *Science*, 2004, **306**, 666–669.

12 J. Choi, K. Kim, B. Kim, H. Lee and S. Kim, *J. Phys. Chem. C*, 2009, **113**, 9433–9435.

13 A. Ismach, C. Druzgalski, S. Penwell, A. Schwartzberg, M. Zheng, A. Javey, J. Bokor and Y. Zhang, *Nano Lett.*, 2010, **10**, 1542–1548.

14 D. Parviz, F. Irin, S. A. Shah, S. Das, C. B. Sweeney and M. J. Green, *Adv. Mater.*, 2016, **28**, 8796–8818.

15 S. Pei and H.-M. Cheng, *Carbon N. Y.*, 2012, **50**, 3210–3228.

16 S. M. Tan, A. Ambrosi, C. K. Chua and M. Pumera, *J. Mater. Chem. A*, 2014, **2**, 10668–10675.

17 N. G. de Barros, A. C. Gonzaga Neto, K. B. Vaccioli, H. R. V. Angulo, L. G. de Andrade e Silva, S. M. Toffoli and T. S. Valera, *C — J. Carbon Res.*, 2023, **9**, 73.

18 M. Coros, F. Pogacean, A. Turza, M. Dan, C. Berghian-Grosan, I.-O. Pana and S. Pruneanu, *Phys. E Low-dimensional Syst. Nanostructures*, 2020, **119**, 113971.

19 A. Capezza, R. L. Andersson, V. Ström, Q. Wu, B. Sacchi, S. Farris, M. S. Hedenqvist and R. T. Olsson, *ACS Omega*, 2019, **4**, 3458–3468.

20 G. K. Ramesha and S. Sampath, *J. Phys. Chem. C*, 2009, **113**, 7985–7989.

21 X. Gao, J. Jang and S. Nagase, *J. Phys. Chem. C*, 2010, **114**, 832–842.

22 S. Mao, H. Pu and J. Chen, *RSC Adv.*, 2012, **2**, 2643–2662.

23 I. I. Edward, N. Abdul Manaf, S. A. Tahir Abdul Muthalib, M. R. Musram Rakunman, L. S. Tan and T. Tsuji, *IOP Conf. Ser. Mater. Sci. Eng.*, 2021, **1142**, 12019.

24 A. Lerf, H. He, M. Forster and J. Klinowski, *J. Phys. Chem. B*, 1998, **102**, 4477–4482.

25 D.-D. Han, Y.-L. Zhang, Y. Liu, Y.-Q. Liu, H.-B. Jiang, B. Han, X.-Y. Fu, H. Ding, H.-L. Xu and H.-B. Sun, *Adv. Funct. Mater.*, 2015, **25**, 4548–4557.

26 C. Yang, J. Gong, P. Zeng, X. Yang, R. Liang, Q. Ou and S. Zhang, *Appl. Surf. Sci. 2018,* **9**, 5334–5340.

27 S. H. Kang, I. G. Kim, B.-N. Kim, J. Sul, Y. Kim and I.-K. You, *ETRI J.*, 2018, **40**, 275–282.

28 L. Chen, Z. Xu, J. Li, C. Min, L. Liu, X. Song, G. Chen and X. Meng, *Mater. Lett.*, 2011, **65**, 1229–1230.

29 H. Guo, M. Peng, Z. Zhu and L. Sun, *Nanoscale*, 2013, **5**, 9040–9048.

30 Y. He, J. Li, L. Li and J. Li, *Mater. Lett.*, 2016, **177**, 76–79.

31 M. Fujitsuka and T. Majima, *J. Phys. Chem. Lett.*, 2011, **2**, 2965–2971.

32 H. Remita, J. Khatouri, M. Tréguer, J. Amblard and J. Belloni, *Zeitschrift fur Phys. D-Atoms Mol. Clust.*, 1997, **40**, 127–130.

33 C. Zhenpeng, C. Coletta, T. Bahry, J.-L. Marignier, J.-M. Guigner, M. Gervais, S. Baiz, F. Goubard and S. Remita, *Mater. Chem. Front.*, 2017, **1**, 879.

34 K. Naghavi, E. Saion, K. Rezaee and W. M. M. Yunus, *Radiat. Phys. Chem.*, 2010, **79**, 1203–1208.

35 Y. Chouli, F. Belkhadem-Mokhtari, S. Abou Zeid, D. Dragoe, R. Saint-Martin, F. Brisset, H. Remita and S. Remita, *Radiat. Phys. Chem.*, 2022, **195**, 110079.

36 C.-H. Jung, Y.-W. Park, I.-T. Hwang, Y.-J. Go, S.-I. Na, K. Shin, J.-S. Lee and J.-H. Choi, *J. Phys. D Appl. Phys.*, 2013, **47**, 5105.

37 C. Ferradini and J.-P. Jay-Gerin, *Can. J. Chem.*, 2011, **77**, 1542–1575.

38 J. Belloni, M. Mostafavi, H. Remita, J.-L. Marignier and and Marie-Odile Delcourt, *New J. Chem.*, 1998, **22**, 1239–1255.

39 A. Henglein, *Berichte der Bunsengesellschaft für Phys. Chemie*, 1991, **95**, 451.

40 M. Von Piechowski, M.-A. Thelen, J. Hoigné and R. E. Bühler, *Berichte der Bunsengesellschaft für Phys. Chemie*, 1992, **96**, 1448–1454.

41 B. Zhang, L. Li, Z. Wang, S. Xie, Y. Zhang, Y. Shen, M. Yu, B. Deng, Q. Huang, C. Fan and J. Li, *J. Mater. Chem.*, 2012, **22**, 7775–7781.

42 H. Zhao, Z. Li, N. Zhang, Y. Du, S. Li, L. Shao, D. Gao, X. Han and P. Xu, *RSC Adv.*, 2014, **4**, 30467–30470.

43 M. Lu, J. Li, L. Li, J. Lin and J. Li, *Fullerenes, Nanotub. Carbon Nanostructures*, 2019, **28**, 1–10.

44 B. Gupta, A. Melvin, T. Matthews, S. Dhara, S. Dash and A. K. Tyagi, *Int. J. Hydrogen Energy*, 2015, **40**(17), 5815-5823.

45 M. Sun, G. Wang, X. Li and C. Li, *J. Power Sources*, 2014, **245**, 436–444.

46 Y.-J. Noh, S.-C. Park, I.-T. Hwang, J.-H. Choi, S.-S. Kim, C.-H. Jung and S.-I. Na, *Carbon N. Y.*, 2014, **79**, 321–329.

47 J. Shi, W. Jiang, L. Liu, M. Jing, F. Li, Z. Xu and X. Zhang, *Curr. Appl. Phys.*, 2019, **19**, 780-786.

48 Y. Zhang, H.-L. Ma, Q. Zhang, J. Peng, J. Li, M. Zhai and Z.-Z. Yu, *J. Mater. Chem.*, 2012, **22**, 13064–13069.

49 A. Ansón-Casaos, J. A. Puértolas, F. J. Pascual, J. Hernández-Ferrer, P. Castell, A. M. Benito, W. K. Maser and M. T. Martínez, *Appl. Surf. Sci.*, 2014, **301**, 264–272.

50 L. SHAHRIARY and A. A. ATHAWALE, *Bull. Mater. Sci.*, 2015, **38**, 739–745.

51 H. Remita, I. Lampre, M. Mostafavi, E. Balanzat and S. Bouffard, *Radiat. Phys. Chem.*, 2005, **72**, 575–586.

52 C. Grupen, *Introduction to radiation protection : practical knowledge for handling radioactive sources*, Berlin ; London, Springer., 2010.

53 G. G. Jayson, B. J. Parsons and A. J. Swallow, *Int. J. Radiat. Phys. Chem.*, 1975, **7**, 363–370.

54 P. Tiamduangtawan and K. Saenboonruang, *J. Phys. Conf. Ser.*, 2019, **1285**, 12034.

55 C. D. Jonah, *Radiat. Res.*, 1995, **144**, 141–147.

56 J. D. Zimbrick, *Radiat. Res.*, 2002, **158**, 127–140.

57 C. Ferradini and J.-P. Jay-Gerin, *Res. Chem. Intermed.*, 2000, **26**, 549–565.

58 Z. D. Draganic and I. G. Draganic, *J. Phys. Chem.*, 1973, **77**, 765–772.

59 H. A. Schwarz and R. W. Dodson, *J. Phys. Chem.*, 1989, **93**, 409–414.

60 S. Remita, Thesis, Paris-Sud University, Orsay, 1995.

61 Y. Yang, L. Chen, D.-Y. Li, R.-B. Yi, J.-W. Mo, M.-H. Wu and G. Xu, *RSC Adv.*, 2019, **9**, 3597–3604.

62 J. Li, G. Xiao, C. Chen, R. Li and D. Yan, *J. Mater. Chem. A*, 2013, **1**, 1481–1487.

63 J. I. Paredes, S. Villar-Rodil, A. Martínez-Alonso and J. M. D. Tascón, *Langmuir*, 2008, **24**, 10560–10564.

64 S. Gurunathan, J. W. Han, V. Eppakayala and J.-H. Kim, *Int. J. Nanomedicine*, 2013, **8**, 1015–1027.

65 A. C. Ferrari and D. M. Basko, *Nat. Nanotechnol.*, 2013, **8**, 235–246.

66 L. M. Malard, D. L. Mafra, S. K. Doorn and M. A. Pimenta, *Solid State Commun.*, 2009, **149**, 1136–1139.

67 D. Graf, F. Molitor, K. Ensslin, C. Stampfer, A. Jungen, C. Hierold and L. Wirtz, *Nano Lett.*, 2007, **7**, 238–242.

68 J. Hong, M. K. Park, E. J. Lee, D. Lee, D. S. Hwang and S. Ryu, *Sci. Rep.*, 2013, **3**, 2700.

69 G. M. de Araújo, L. Codognoto and F. R. Simões, *J. Solid State Electrochem.*, 2020, **24**, 1857–1866.

70 R. Rozada, J. Paredes, S. Villar-Rodil, A. Martínez-Alonso and J. Tascón, *Nano Res.*, 2013, **6**, 216–233.

71 M. Boutchich, A. Jaffré, D. Alamarguy, J. Alvarez, A. Barras, Y. Tanizawa, R. Tero, H. Okada, T. V Thu, J. P. Kleider and A. Sandhu, *J. Phys. Conf. Ser.*, 2013, **433**, 12001.

72 Y. Dai, Y. Jing, J. Zeng, Q. Qi, C. Wang, D. Goldfeld, C. Xu, Y. Zheng and Y. Sun, *J. Mater. Chem.*, 2011, **21**, 18174–18179.

73 A. A. K. King, B. R. Davies, N. Noorbehesht, P. Newman, T. L. Church, A. T. Harris, J. M. Razal and A. I. Minett, *Sci. Rep.*, 2016, **6**, 19491.

74 M. Mokhtar, S. Abo-El-Enein, M. Hassaan, M. Morsy and M. H. Khalil, *Int. J. Nanoparticles Nanotechnol.*, 2017, **3**:008.

75 S. Some, Y. Kim, Y. Yoon, H. Yoo, S. Lee, Y. Park and H. Lee, *Sci. Rep.*, 2013, **3**, 1929.

76 B. Rajagopalan and J. S. Chung, *Nanoscale Res. Lett.*, 2014, **9**, 535.

77 A. Lee, K. Yang, D. A. Nguyen, C. Park, S. Lee, T. Lee and M. S. Jeong, *Appl. Surf. Sci.*, 2021, **536**, 147990.

78 G. Wei, J. Yu, M. Gu and T. Tang, *J. Appl. Phys.*, 2016, **119**, 224102.

79 J. C. Silva Filho, E. C. Venancio, S. C. Silva, H. Takiishi, L. G. Martinez and R. A. Antunes, *SN Appl. Sci.*, 2020, **2**, 1450.

80 T. Szabó, O. Berkesi and I. Dekany, *Carbon N. Y.*, 2005, **43**, 3186–3189.

81 C. Manoratne, S. Rosa and I. Kottegoda, *Mater. Sci. Res. India*, 2017, **14**, 19–30.

82 H.-L. Guo, X.-F. Wang, Q.-Y. Qian, F.-B. Wang and X.-H. Xia, *ACS Nano*, 2009, **3**, 2653–2659.

83 P. Khanra, T. Kuila, N. H. Kim, S. H. Bae, D. Yu and J. H. Lee, *Chem. Eng. J.*, 2012, **183**, 526–533.

84 B. D. Ossonon and D. Bélanger, *RSC Adv.*, 2017, **7**, 27224–27234.

85 J. Zhang, Y. Xu, Z. Liu, W. Yang and J. Liu, *RSC Adv.*, 2015, **5**, 54275.

86 R. Al-Gaashani, A. Najjar, Y. Zakaria, S. Mansour and M. A. Atieh, *Ceram. Int.*, 2019, **45**, 14439–14448.

87 C. K. Chua and M. Pumera, *J. Mater. Chem.*, 2012, **22**, 23227–23231.

88 N. Díez, A. Śliwak, S. Gryglewicz, B. Grzyb and G. Gryglewicz, *RSC Adv.*, 2015, **5**, 81831–81837.

89 E. Aliyev, V. Filiz, M. M. Khan, Y. J. Lee, C. Abetz and V. Abetz, *Nanomater. (Basel, Switzerland)*, 2019, **9**, 1180.

90 M. Wah, T. Aung and W. Htwe, *Electrical Properties of Chemically Reduced Graphene Nanosheets*, 2018.

91 S. Drewniak, T. Pustelny, R. Muzyka and A. Plis, *Polish J. Chem. Technol.*, 2015, **17**, 109.

92 A. Shalaby, D. Nihtianova, P. Markov, A. Staneva, R. Iordanova and Y. Dimitriev, *Bulg. Chem. Commun.*, 2015, **47**, 291–295.

93 D. Suresh, N. P C, U. Gowda, N. Bhushana and S. Sharma, *Ceram. Int.*, 2015, **41**, 4810–4813.

94 F. Farivar, P. Lay Yap, R. U. Karunagaran and D. Losic, *C*, 2021, **7**, 41.

95 N. Kumar and V. C. Srivastava, *ACS Omega*, 2018, **3**, 10233–10242.

96 A. Ambrosi, C. K. Chua, A. Bonanni and M. Pumera, *Chem. Rev.*, 2014, **114**, 7150–7188.

97 M. D. Stoller, S. Park, Y. Zhu, J. An and R. S. Ruoff, *Nano Lett.*, 2008, **8**, 3498–3502.

98 P. Krishnan and V. Biju, *Bull. Mater. Sci.*, 2021, **44**, 288.

99 Y. Chen, X. Zhang, D. Zhang, P. Yu and Y. Ma, *Carbon N. Y.*, 2011, **49**, 573–580.

100 L. W. Le Fevre, J. Cao, I. A. Kinloch, A. J. Forsyth and R. A. W. Dryfe, *ChemistryOpen*, 2019, **8**, 418–428.

101 J. Yang and S. Gunasekaran, *Carbon N. Y.*, 2013, **51**, 36–44.

102 D. Sun, X. Yan, J. Lang and Q. Xue, *J. Power Sources*, 2013, **222**, 52–58.

103 W. Shi, J. Zhu, D. H. Sim, Y. Y. Tay, Z. Lu, X. Zhang, Y. Sharma, M. Srinivasan, H. Zhang, H. H. Hng and Q. Yan, *J. Mater. Chem.*, 2011, **21**, 3422–3427.

104 S. R. C. Vivekchand, C. S. Rout, K. S. Subrahmanyam, A. Govindaraj and C. N. R. Rao, *J. Chem. Sci.*, 2008, **120**, 9–13.

105 B. Pal, S. Yang, S. Ramesh, V. Thangadurai and R. Jose, *Nanoscale Adv.*, 2019, **1**, 3807–3835.

106 Y. Hernandez, M. Lotya, D. Rickard, S. D. Bergin and J. N. Coleman, *Langmuir*, 2010, **26**, 3208–3213.

107 J. Dai, G. Wang, L. Ma and C. Wu, *J. Mater. Sci.*, 2015, **50**, 3895–3907.

108 D. Konios, M. M. Stylianakis, E. Stratakis and E. Kymakis, *J. Colloid Interface Sci.*, 2014, **430**, 108–112.

109 U. Khan, H. Porwal, A. O'Neill, K. Nawaz, P. May and J. N. Coleman, *Langmuir*, 2011, **27**, 9077–9082.

110 S. Wang, Y. Zhang, N. Abidi and L. Cabrales, *Langmuir*, 2009, **25**, 11078–11081.